

A New Ray-Tracing-Assisted Calibration Method of a Fiber-Optic Thickness Probe for Measuring Liquid Film Flows

メタデータ	言語: eng 出版者: 公開日: 2021-10-15 キーワード (Ja): キーワード (En): 作成者: Mizushima, Yuki メールアドレス: 所属:
URL	http://hdl.handle.net/10297/00028392

A new ray tracing assisted calibration method of a fiber-optic thickness probe for measuring liquid film flows

Yuki Mizushima

Abstract—A ray-tracing-assisted (RTA) method for calibrating a fiber-optic thickness probe (FOTP) that enables the measurement of thickness in micrometers in wavy liquid-film flow is described herein. This technique calibrates the device more quickly than other liquid-film measurements and more efficiently than conventional fiber-optic methods. First, the emission natures of the multimode optical fiber were investigated through ray tracing. The step-index multimode fiber was observed to be superior to the graded-index multimode fiber regarding the thickness resolution and the uncertainty avoidance of the liquid-film shape. Second, the RTA calibration method for pseudo-thickness measurement under stagnant conditions was validated. The measured thickness of the calibrated FOTP was compared to that of visualization. Agreement between the two resulted in a maximum difference of 10% for over 200 μm and 20% for under 200 μm . Finally, the numerical verification of this method in virtual liquid-film flow was demonstrated. The applicable thickness range and measurement uncertainty of the FOTP, which are unattainable by experiments alone, are discussed.

Index Terms—calibration, fluid flow measurement, liquids, optical fiber sensors, ray tracing, thickness measurement

I. INTRODUCTION

A liquid-film flow with an inseparable relationship to the mass/heat transfer through a gas-liquid interface [1-10] is increasingly important to manufacturers, as it will allow further efficient and safe operations of fluid machines for a sustainable future. There is an increasing demand for the direct diagnosis of liquid-film flows with thickness ranging from 1 to 500 μm (hereafter referred to as microfilm flow); for example, the liquid-film formation in a steam turbine [11-14], the wafer deposition of semiconductor processing [15], and the lubrication of bearings [16]. General thickness measurements based on interferometry [17,18] and polarization [19] are mainly static methods; it is challenging to measure the thickness in motion. In addition, the diagnosis requires sufficient resolutions of time, space, and thickness to reveal the flow structure, since complex waves often accompany a microfilm flow, the wavelength and frequency of which are very important information in transport phenomena [20]. No such in-situ method has been developed.

Table I shows some promising methods that involve no contamination and less invasiveness. The ultrasonic echo technique (UET) [21], a laser focusing distance meter (LFD) [22], and X-ray tomography [23] are noninvasive methods. X-ray tomography requires calibration, but the relative error can be smaller than those of the other measurements, because of the fewer external factors contributing to the measurement error [24]. While these techniques have excellent features, they should be performed in a well-equipped environment, such as a laboratory. The constant electric current method (CECM) [25] and a fiber-optic thickness probe (FOTP) [26,29,30] are easier to install in fluid machines. An optical fiber has durability in an aggressive environment, thereby achieving various challenging applications [31-37]. The FOTP method is thus expected to become more widely applicable and reliable for the direct diagnosis of liquid-film flows compared to the other techniques. However, the measurement uncertainty with an FOTP is large when the thickness ranges in the micrometers [30]. This is because the conventional studies have aimed at measuring the mm-order thickness of the liquid film and just implied FOTP's applicability to micron thickness. The models of the thickness-vs.-signal are not robust yet; an FOTP therefore often requires a careful, accurate, and precise calibration experiment prior to being used for thickness measurements.

To improve the accuracy of an FOTP for microfilm flows, a new ray-tracing-assisted (RTA) calibration method has been developed. In this study, the thickness measurements by FOTPs were first simulated by a full three-dimensional ray-tracing simulation [35-38]. The light distribution from the fiber tip and calibration plots were numerically obtained and analyzed. The simulated FOTPs were of three types: a conventional cylinder sensor made of graded-index multimode (GI) fiber, a cylinder sensor of step-index multimode (SI) fiber, and a wedge-shaped sensor of the SI fiber. Second, the RTA calibration procedure was established. Third, the RTA calibrations were empirically validated. The distance from the interface to the FOTP was visualized and then compared with the values measured by the calibrated FOTPs. Agreement between the two resulted in a maximum difference of 10% for over 200 μm and 20% for under 200 μm , including bias and random errors. Lastly, the

This work was supported by JSPS KAKENHI Grant Number JP20K14647. Yuki Mizushima is with the Department of Mechanical Engineering, Graduate School of Integrated Science and Technology, Shizuoka University, 3-5-1

Johoku, Naka-ku, Hamamatsu, Shizuoka 432-8561, Japan (e-mail: mizushima.yuhki@shizuoka.ac.jp).

TABLE I
CONVENTIONAL MEASUREMENT METHODS FOR MICROFILM FLOWS

	UET (external scan)	LFD	X-ray tomography	CECM	FOTP
Measurement variable	Transit time through a distance L_{fm}	Translation distance, Δx	X-ray attenuation, ΔI	Potential difference, ΔV	Distance attenuation, ΔI
Spatial resolution	< (transducer size)	> (laser spot size)	< (pixel size)	> (electrode distance)	> (fiber diameter)
Temporal resolution	$(L+L_{fm})/C$	$1/f_{sample}$	$1/f_{sample}$	$1/f_{sample}$	$1/f_{sample}$
Thickness resolution	$C/2f_{sample}$	$\sim (A/D \text{ resolution})$	$\sim (A/D \text{ resolution})$	$\sim (A/D \text{ resolution})$	$\sim (A/D \text{ resolution})$
Relative error	$\sim C/L_{fm}f_{sample}$	$\sim \varepsilon_x/L_{fm}$	$\sim \varepsilon_I/\Delta I(L_{fm})$	$\sim \varepsilon_V/\Delta V(L_{fm})$	$\sim \varepsilon_I/\Delta I(L_{fm})$
Needs calibration?	No	No	Yes	Yes	Yes
Initial cost	9,000 USD	14,000 USD	100,000 USD~	28,000 USD	6,800 USD
Invasiveness	Non-invasive	Non-invasive*	Non-invasive	Semi-invasive	Semi-invasive

*an exception is that LFD needs a window if not the transparent channel. I (-): electromagnetic wave intensity, L_{fm} (m): liquid-film thickness, f_{sample} (Hz): sampling rate, L (m): wall thickness, C (m/s): speed of sound in water, ε_I (-): uncertainty in X-ray intensity, ε_V (V): uncertainty in signal level, ε_x (-): uncertainty in position

liquid-film flow measurement was virtually demonstrated through the ray tracing, and then the uncertainty and applicable thickness range of the FOTPs are discussed. This study not only contributes to the improvement of the accuracy of FOTPs; it also extends the possibility of the optical measurement hidden in the experiment.

II. THE FIBER-OPTIC THICKNESS PROBE

The principle of an FOTP is based on the relationship between the local liquid-film thickness and the intensity of the reflection at the gas-liquid interface [38]. A system for the optical sensor is shown in Fig. 1. The laser beams from a laser diode (1) pass through a beam splitter (2) and are focused by an objective lens (3). The beams reaching the end of the tip fixed at the channel base are refracted and emitted into the liquid, then reflected at the gas-liquid interface (glare) and subsequently returned into the same fiber. The glare beams are entered into a photomultiplier (6) through a beam splitter and a polarizer (5). The output signal obtained from the photomultiplier (glare signal) is recorded in a personal computer (PC) (7). When the distance from the tip to the interface is small (Fig. 2a), the intensity of the glare beams is large, i.e., the output voltage is high. When the distance is large (Fig. 2b), most of the glare beams are dispersed into the liquid phase, and the output voltage is low. We can measure the distance as a film thickness, L_{fm} , by using coefficients of the distance and recorded output voltage.

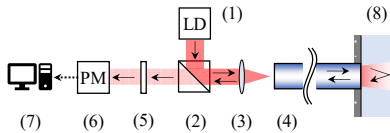


Fig. 1. Optical configuration of the FOTP, with the (1) laser diode, (2) beam splitter, (3) objective lens, (4) ORP, (5) polarizer, (6) photo multiplier, (7) PC, (8) liquid film.

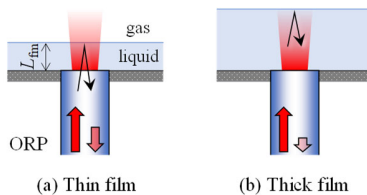


Fig. 2. Measurement principle of the FOTP.

III. RAY-TRACING SIMULATOR

With the conventional FOTP, a calibration experiment is required [30] prior to measuring the microfilm flow. This would require the realization of Fig. 2 at micrometric resolution, which is not an easy experiment to conduct. More efficient and reasonable calibration is desirable. In addition, we must obtain the calibration curve from the empirical plots with proper interpolation. In this context, a physical model of the FOTP is very necessary. Otsu and his group successfully obtained the calibration curve of GI fibers by performing an experiment and 2D geometric analysis [26]. There has been little progress in terms of the models for the FOTP. The difficulty in the modelling is how to simulate the multiscale propagation ranging from micrometers to several tens of centimeters as the depicted optical path in Fig. 1. The measurement variable is only the intensity through the fiber; therefore, the most important matter is where and what amount of light are refracted/reflected. The ray tracing is thus a suitable tool for this specific aim.

Ray tracing is a well-known geometric optics technique [39] that obeys the ray equation simplified from the Maxwell equation: the ray segments are transmitted straight in a homogeneous media. The underlying concepts are illustrated in Fig. 3. The three-dimensional ray tracing for fluid measurement with an optical fiber was originated by Sakamoto and Saito [35], who discussed their analysis of the measured signal in a dispersed two-phase flow and the method's validity in detail.

According to Fig. 3, the angles of refraction and reflection are quantified on the interfaces by following Snell's law,

$$\frac{\sin \theta_t}{\sin \theta_i} = \frac{n_i}{n_t} \quad (1)$$

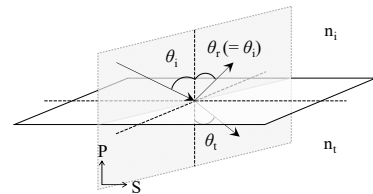


Fig. 3. Schematic of ray tracing. θ_i : the incoming angle, θ_r : the reflecting angle, θ_t : the refracting angle, n_i : the refractive index of the incoming media, n_t : the refractive index of the transmitting media.

The energy of reflectivity and transmissivity are obtained by the following equations derived from Fresnel's equation, assuming the interfaces are enough smooth to neglect random reflection.

$$R_P = \frac{\tan^2(\theta_i - \theta_t)}{\tan^2(\theta_i + \theta_t)} \quad (2)$$

$$R_S = \frac{\sin^2(\theta_i - \theta_t)}{\sin^2(\theta_i + \theta_t)} \quad (3)$$

$$T_P = \frac{\sin(2\theta_i)\sin(2\theta_t)}{\sin^2(\theta_i + \theta_t)\cos^2(\theta_i - \theta_t)} \quad (4)$$

$$T_S = \frac{\sin(2\theta_i)\sin(2\theta_t)}{\sin^2(\theta_i + \theta_t)} \quad (5)$$

where R is reflectivity, T is transmissivity, and P and S indicate parallel and perpendicular (senkrecht) polarization, respectively.

IV. METHODS

A. Simulated models and conditions for calibration plots

Three types of the FOTP were examined: a cylindrical SI fiber (0S); a 30deg.-wedge-shaped SI fiber (1S); and a cylindrical GI fiber (0G). The simulated models consisted of 3-INTERFACES; a cut cylinder, an ellipse, and a midair ellipse, and 5-BODYS; phase 1, phase 2, fiber core, fiber clad, and outside as depicted in Fig. 4. First, 10,000 rays are introduced from the surface-(v) followed with NA=0.22 of the fiber, then glare rays returning to (v) are collected at each distance from the surface-(vi) to -(ix), L_{fm} ($= 0.1 \mu\text{m}$ and 10 to 1000 μm in 10 μm increments). Interface's inclination ϕ_{fm} and position θ_{fm} (for 1S) are defined in every L_{fm} as illustrated in Fig. 5 ($0 < \phi_{fm} \leq 90$ deg. and $0 \leq \theta_{fm} \leq 180$ deg. in 5 deg. increments). Thus, a relationship between the glare-light intensity and L_{fm} is obtained. Figs. 6 and 7 show the calculation procedure. Note that the propagation through the GI fiber complies with Ohba's hypothesis [26].

B. Experimental validation: Quiescent-film measurement

Based on the calibration data, the measured thickness in a quiescent condition via the FOTP is compared with shadowgraph [27]. It is preferable to confirm the liquid-film measurement of Fig. 1 in as similar conditions as possible. The FOTP should therefore be positioned in the internal medium of a larger refractive index (RI) than the external medium. Moreover, there must not be any obstacles to the visualization.

Ultrapure water (Milli-Q, Millipore), RI=1.333 measured by a pocket refractometer (PAL-RI, Atago), and mineral oil (Sigma-Aldrich), RI=1.469, are separately filled in a single plastic cuvette (10 mm \times 10 mm \times 45 mm) at room temperature. The denser water stays under the oil, and the oil-water interface forms as in a density experiment. The inside of the cuvette is partly coated with an oleophilic substance (Glaco Blave, Soft99), and thus the interface takes a loosely convex shape upward. The camera can therefore visualize the interface at the micron-level very clearly; otherwise, the interface is hidden by the concave meniscus (Fig. 8). The captured images are binarized [28], then the distance from the FOTP and the

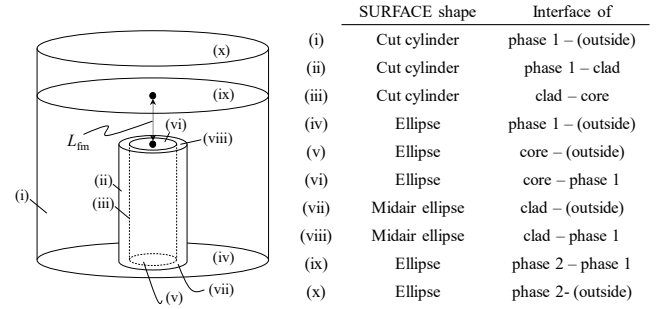


Fig. 4. Definition of the simulated model: INTERFACES and BODYS.

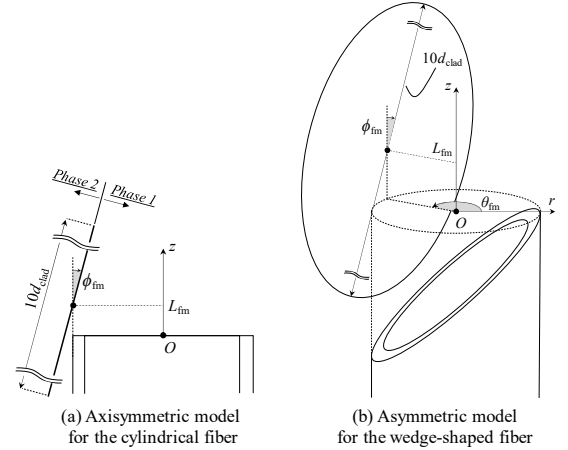


Fig. 5. Schematic of the raytracing models, where (a) for cylindrical type (0S and 0G) and (b) for wedge-shaped type (1S).

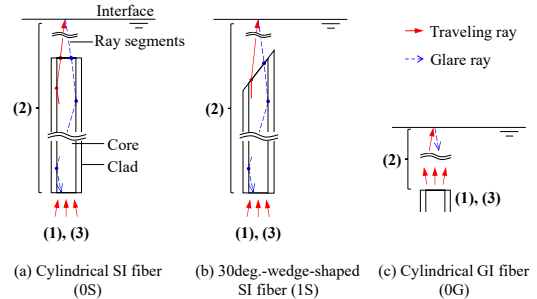


Fig. 6. Graphical procedures of the calculation. The numbers in brackets correspond to Fig. 7.

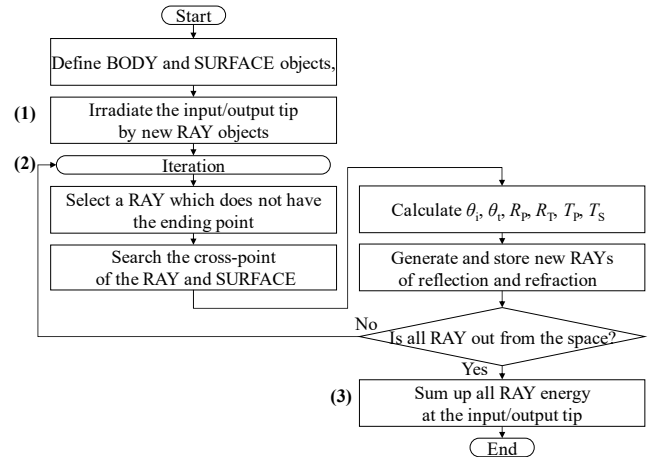


Fig. 7. Flowchart of the raytracing.

interface is measured. The experimental apparatus is illustrated in Fig. 10a. An SI fiber (diameter of the fiber core (d_{core}) and clad (d_{clad}): 100 μm /140 μm and RI of the core/clad: 1.457/1.440, AFS100/140T, Fiberguide Industries) is inserted into the stainless steel tube, fixed on a 3-axis motorized stage (KS362-100 and KS162-50, Suruga Seiki), and its position was controlled. The camera (D750, Nikon) with a 300mm f/2.8 lens (NIKKOR, Nikon) captures two directional images at once by using a prism (DPB-30-10H, Sigmakoki) and flat mirrors (Edmund Optics). A metal halide lamp (MME-250, Moritex) is used as the light source. The right side of the camera view is an image visualized from the x -direction, and the left side is from the y -direction (Fig. 9b,c). The FOTP is set out above the flat part of the interface at $L_{\text{fm}}=1000 \mu\text{m}$, then moved along the z -direction closer to the interface, step by step. The delivered glare light from the fiber is converted to the electric signals by a photomultiplier (R928, Hamamatsu Photonics) and recorded at each step. Fig. 10 provides a micrograph of the examined FOTPs' tip.

C. Numerical verification: Virtual film flow measurement

This section shows how to demonstrate the wavy micro-film flow measurement with the raytracing method. First, (6) and (7) generate a random wave.

$$\delta(t) = 2 \sum_{i=0}^{100} \left\{ \sqrt{S(\bar{\omega}_i) \Delta\omega_i} \cos(\bar{\omega}_i t - \varphi_i) \right\} \quad (6)$$

$$S(\omega) = 2AB \left\{ \frac{1}{B^2 + (\omega + \omega_0)^2} + \frac{1}{B^2 + (\omega - \omega_0)^2} \right\} \quad (7)$$

where δ is the wave height, t is the time, i is the waveform number, S is a spectrum, ω is an angular frequency, φ_i is a phase, A and B are constant numbers, $\bar{\omega}_i = (\omega_i + \omega_{i-1})/2$, and $\Delta\omega_i = \omega_i - \omega_{i-1}$. Random numbers from 0 to 1 are substituted for ω_i and φ_i , respectively. This random wave is divided into N segments and has a complete length of $(N-1)W_{\text{fm}}$, where W_{fm} is the interval length. Here, W_{fm} is defined by d_{clad} for evaluating an uncertainty of the local curvature of the interface: $0.1d_{\text{clad}}$, d_{clad} , and $10d_{\text{clad}}$. Next, $(N-1)$ INTERFACES of rectangle are coupled next to each other (Fig. 11). The FOTP is fixed at the center of the interface, and then the glare light intensity is calculated. Neglecting the dispersion, the random wave moves $\Delta x (=d_{\text{clad}})$ toward the longitudinal direction in every calculation. Finally, according to the calibration data, the signal is converted to a time-series thickness variation.

V. RESULT AND DISCUSSION

A. Glare-light characteristics and calibration procedure

1) Emission- and glare-intensity distributions

The calculated results are summarized in Figs. 12–14. The calculation condition has been applied correspondingly to the experiment: the shape and dimensions of the FOTPs and the RI of the phase1/phase2 (1.469/1.333).

According to Fig. 12, the ray intensity distributions are different from each fiber-species. The emissions from the SI fibers have larger areas of high intensity than that of the GI fiber.

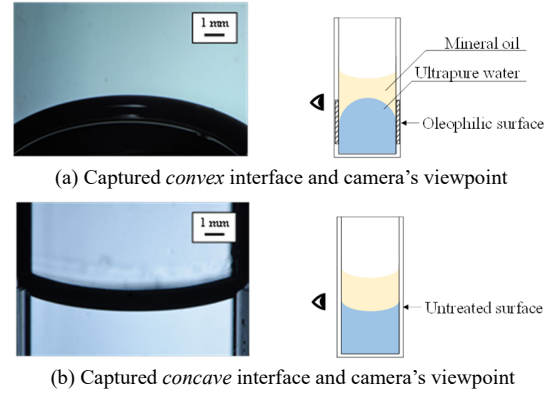
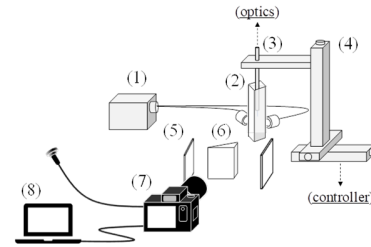


Fig. 8. Surface pretreatment for the wettability of the plastic cuvette. The contact angle of the oil-water interface on the cuvette surface was normally <90 deg. and thus the interface formed a concave shape. The distance of the fiber's tip and interface is hidden in this situation. By coating the surface with an oleophilic substance, the contact angle became >90 deg., and then the interface forms a convex shape. The distance was thus successfully visualized.



(a) Experimental apparatus, (1) metal halide lamp, (2) cuvette, (3) FOTP, (4) 3-axis motorized stage, (5) flat mirrors, (6) prism, (7) camera, (8) PC.

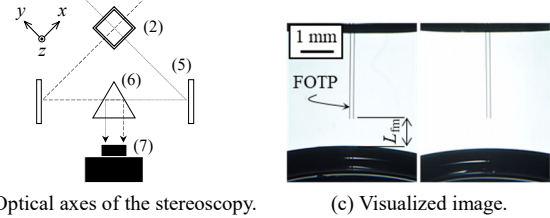


Fig. 9. The experimental apparatus and visualization method.

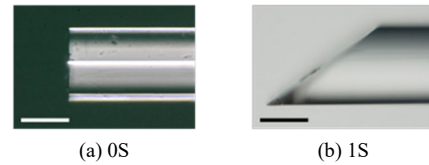


Fig. 10. Micrographs of the examined FOTP. Square bars = 100 μm .



Fig. 11. Definition of the simulated model (not too scale).

This arises from a difference in the design concepts of the fibers. The SI fiber is the simplest fiber whose RI is constant in the core; therefore, the light uniformly emits from the SI fiber core [38,40], like surface-emission. In contrast, the RI of the core in the GI fiber is non-uniform for reducing the aberration during propagation. The RI is higher at the axis of the core and continuously decreases along the radial direction, and thus the emission follows the Gaussian beams' nature, the same as the introduced laser. The predicted relationship between the glare intensity I_G and L_{fm} (Fig. 13) reflects the emission characteristics. Every I_G monotonically decreases as the L_{fm} increases, following the inverse square law. However, a different relationship is observed at $L_{fm}/d_{core} < 3$ of 0S- and 1S-type and at $L_{fm}/d_{core} < 0.5$ of 0G-type, respectively, where d_{core} is the diameter of the fiber's core. These lengths correspond to the high-intensity region of the emission in Fig. 12; therefore, the detected I_G steeply decreases near the tip of 0S and 1S [38]. In contrast, I_G inevitably saturates at close to the 0G's tip.

Fig. 14 shows the I_G distribution in L_{fm} , ϕ_{fm} and θ_{fm} . Note that the values along dashed lines in the figure's panels (b), (d) and (f) correspond to Fig. 13. The area of $I_G > 0.9$ of 0S and 1S is very small compared to that of 0G. This is attributable to the emission nature of the SI fiber as mentioned above. In addition, the distribution of 1S exhibits an asymmetric profile due to the refraction at the wedged surface. 0S and 1S have high sensitivity for thin films $L_{fm} < 2d_{core}$. Moreover, the uncertainty of ϕ_{fm} is much smaller than that for 0G. This is a conventional problem of the FOTP. Even $I_G = 0.9$ was used as a threshold, it was impossible to determine whether there is a film of $L_{fm} = d_{core}$ and $\phi_{fm} = 0$ deg. or a film of $L_{fm} < d_{core}$ and $\phi_{fm} = 10$ deg. (see Fig. 14f). However, 0S and 1S can remarkably decrease this uncertainty, which indicates that they are preferable for quantitatively measuring the thickness of the microfilm flow.

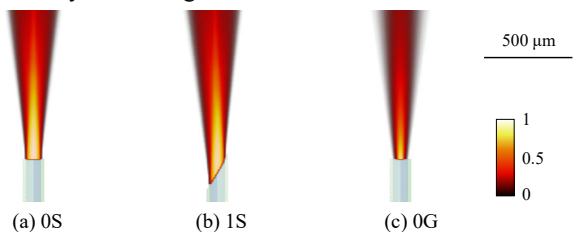


Fig. 12. Emission intensity distribution of FOTP. All results are plotted as pseudo-color images with ParaView. The color bar indicates normalized value of each sensor.

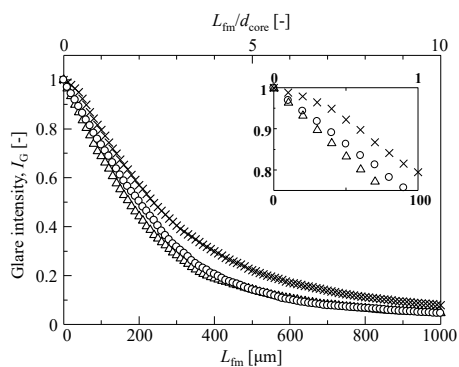


Fig. 13. I_G vs. L_{fm} for 0S (circles), 1S (triangles) and 0G (crosses). The inset indicates $L_{fm} \leq 100 \mu\text{m}$. All results are normalized by each maximum value at $L_{fm} = 0.1 \mu\text{m}$.

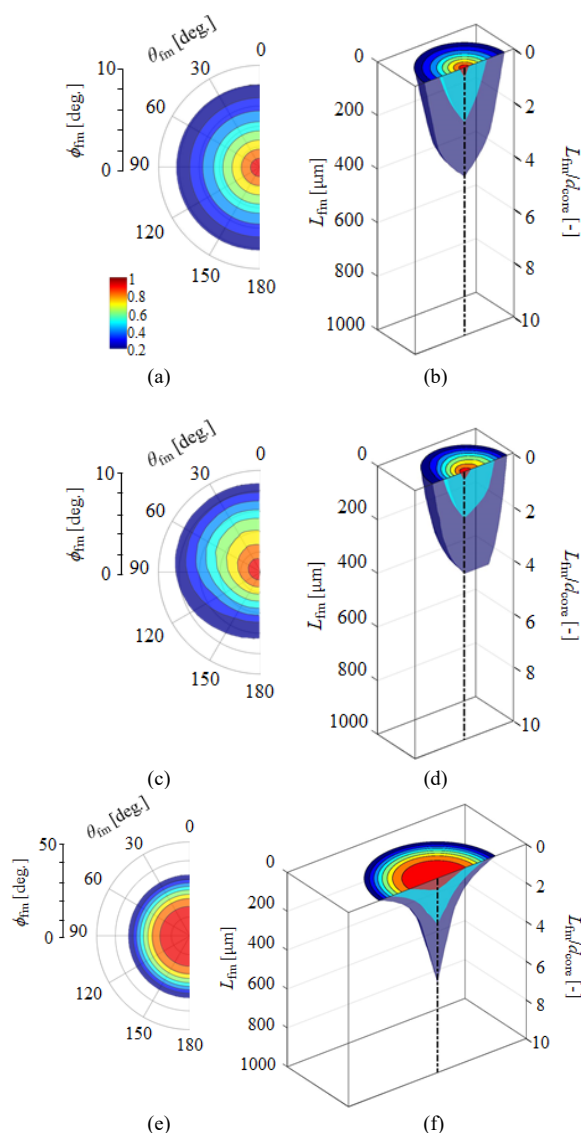


Fig. 14. Contour map of I_G vs. L_{fm} , ϕ_{fm} and θ_{fm} . Upper: 0S, middle: 1S, lower: 0G results. (a), (c) and (e) are at $L_{fm} = 0.1 \mu\text{m}$ and (b), (d) and (f) are $0.1 \mu\text{m} \leq L_{fm} \leq 1000 \mu\text{m}$ which illustrates isosurfaces of $I_G = 0.9$ (red), 0.5 (cyan), 0.2 (navy). All results are normalized by each value at $L_{fm} = 0.1 \mu\text{m}$.

2) Ray-tracing-Assisted (RTA) calibration

Based on the result, we can estimate L_{fm} from the measured glare intensity V_G , which is an output of the optical intensity meter (the photomultiplier, photodetector, power meter, and so on) as the following procedure.

--I. Obtaining the calibration dataset, I_{p1} , and I_{p2} via ray-tracing simulation (Fig. 15).

This is the relationship between L_{fm} (horizontal axis) and I_G (secondary vertical axis). Here, I_{p1} and I_{p2} correspond to I_G at $L_{fm} = \infty \mu\text{m}$ and $0 \mu\text{m}$.

--II. Recording output signals of V_{p1} and V_{p2} delivered from the probe positioned in the phase 1 and the phase 2 (Fig. 16).

--III. Converting non-dimensional intensity I_G to V_G of the arbitrary unit by following equation.

$$\frac{V_G - V_{p1}}{V_{p2} - V_{p1}} = \frac{I_G - I_{p1}}{I_{p2} - I_{p1}} \quad (8)$$

The thickness can be thus evaluated from measured values of V_G by means of the relationship between L_{fm} (horizontal axis) and V_G (primary vertical axis) in Fig. 15.

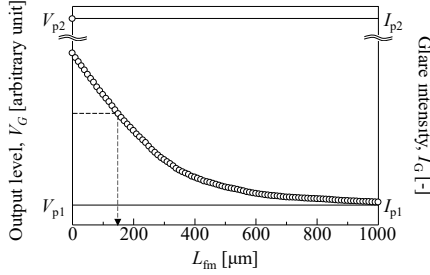


Fig. 15. RTA calibration dataset of 0S-type FOTP for oil-water film.

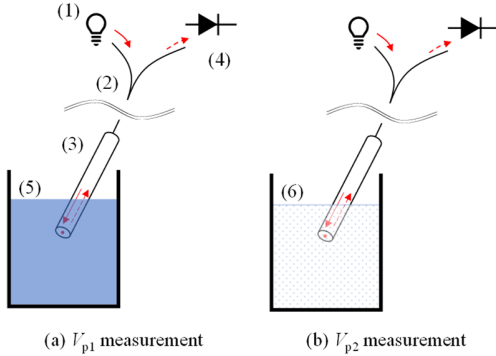


Fig. 16. RTA calibration procedure. (1) light source, (2) 1×2 fiber coupler, (3) FOTP, (4) photodetector, (5) working liquid (phase 1), (6) working liquid or gas (phase 2). The cuvette is large enough and is made of black material that avoids the light reflection from its side and bottom.

This RTA calibration is a much simpler method than the past calibration methods that require dozens of measurements. The important task is to prepare the I_G and L_{fm} dataset in advance according to the RI of the phases and the properties of the optical fiber (i.e., the core and cladding diameters, RI, NA, etc.). It is also good to optimize the FOTP for the target thickness at this stage. Since the computational load for the ray tracing is small in this case, the number of step sizes should be based on the resolution of the intensity meter.

B. Experimental validation: Quiescent-film measurement

Fig. 17 illustrates the results of the verification experiment shown in Fig. 11. The verification was performed with 0S and 1S, to which the RTA calibration is applied. The lateral line is the result of the visualization, and the vertical line is that of the FOTP. The dotted lines are the $\pm 10\%$ range of each value. According to this, 10% or less difference is observed when $L_{fm} > 200 \mu\text{m}$. On the other hand, the difference is 20% when $L_{fm} < 200 \mu\text{m}$. Although there are still some improvements to be made in $L_{fm} < 200 \mu\text{m}$, the validity of this new RTA calibration method has been successfully demonstrated through the experiment.

The tendency of overestimation and underestimation is reversed at the L_{fm} of about $300 \mu\text{m}$. This is the point where the tails of the light-distribution are in Fig. 12, and it is an inflection point of the relationship between I_G and L_{fm} in Fig. 13. This position is a function of the d_{core} , RI, and NA of the optical fiber under ideal conditions. However, misalignment at the input end of the fiber causes a small shift of this position in the optical axis and the radial direction of the fiber under real conditions, resulting in a deviation from the RTA calibration dataset. The fiber-launch system used in this study was manual, and we cannot deny the possibility of imperfect alignment.

In addition, the difference in results between the visualization and FOTP increased when $L_{fm} < 200 \mu\text{m}$. The improved sensitivity to thin films by using SI fibers has increased the sensitivity to noise signals as well. For example, a 10% misreading of the output level can cause evaluation errors of $L_{fm} \pm 50 \mu\text{m}$ regarding $< 200 \mu\text{m}$ in thickness. It should be noted that the signal stability of the photodetector becomes very important [29] in this thickness range.

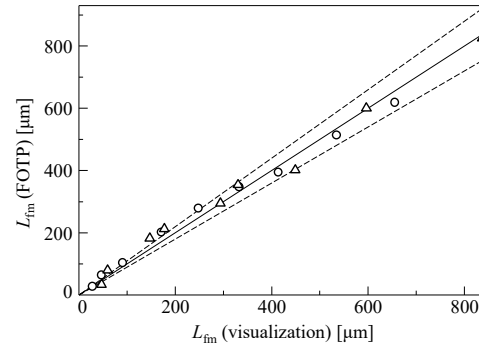


Fig. 17. Validation results of 0S (circles) and 1S (triangles).

C. Numerical verification: Virtual-film-flow measurement

The conventional uncertainty of ϕ_{fm} decreased due to the use of 0S and 1S. In fact, the main concern in thickness measurements of microfilm flows is the uncertainty derived from the local interface shape. The degree to which the local shape affects the FOTP measurement is thus considered with the virtual-film-flow measurement shown in Fig. 8. This analysis was virtually performed with 0S and 1S via the ray-tracing simulator.

Here, Fig. 18 is another calibration dataset for the water/air interface, anticipating a gas-liquid environment where a microfilm flow generally arises. If researchers measure the microfilm flow using the same fiber as in this study, this would be useful for RTA calibration. Although the tendency is almost like that shown in Fig. 13, the sensitivity to L_{fm} near the interface is different, because the distribution of the emitted light in water is different from that in oil. Fig. 19 is a random wave defined by (6) and (7) which has no dispersion and is mathematically easy to describe. It is configured with rectangular elements and thus denoted the horizontal axis as the *ID number of elements*. Three conditions are provided: $0.1d_{\text{clad}}$, d_{clad} , and $10d_{\text{clad}}$. The continuous I_G signal is then obtained when the liquid film is moved sequentially (see the Suppl. Movie).

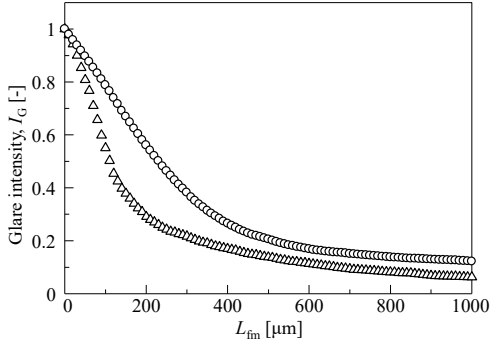


Fig. 18. I_G vs. L_{fm} of 0S (circles) and 1S (triangles) for the water/air interface.

Fig. 20 and Table II show the results. They represent the precise features and limitations of the 0S-type FOTP. When $W_{fm} = 10d_{clad}$ and $W_{fm} = d_{clad}$ (Fig. 20a,b), L_{fm} is slightly overestimated. In addition, some peaks exist during the detection of a thick film, i.e., over 500 μm . These are due to the remaining uncertainty of ϕ_{fm} . It is still difficult to distinguish whether there is a film of $L_{fm} = 500 \mu\text{m}$ and $\phi_{fm} = 0 \text{ deg.}$ or a film of $L_{fm} = 1000 \mu\text{m}$ and $\phi_{fm} = 10 \text{ deg.}$ (Fig. 14b,d). However, this is negligible for a thickness less than 500 μm ; therefore, 0S is a perfect FOTP for the microfilm flow. On the other hand, when $W_{fm} = 0.1d_{clad}$ (Fig. 20c), the thickness measurement becomes very difficult. This means that the local curvature radius of the interface approximately equals d_{clad} . In this situation, the relationship between I_G and L_{fm} becomes indefinite.

The results of the 1S are generally the same as those of the 0S, but the measured L_{fm} is larger than that obtained with 0S. This is because of the uncertainty of ϕ_{fm} derived from the asymmetry of the emitted light. The highest I_G is observed at the interface tilted from the axis of the 1S (Fig. 14c). The 1S positions in the orientation shown in Fig. 8a, and therefore I_G peaks just before the wavefront reaches the bottom. This characteristic is important in terms of the detection for a liquid-film flow with a specific waveform such as a disturbance wave [4], roll wave [5], or breakage [9]. These waves are very significant information, but 0S (including any conventional methods) cannot detect them correctly since their local curvature radius of the interface is small and very complex. 1S has sensitivity that is superior to that of 0S for the waves of films with thickness less than 100 μm , in fact. In this context, 1S is the optimal sensor for complex wave detection.

VI. CONCLUSION

The RTA calibration method of an FOTP has been developed, validated, and verified, to originate a measurement of micron thickness in a flow. This simple procedure can provide an effortless diagnosis. The major uncertainty is due to the local curvature radius of the interface. The waveform is almost replicated if the wavelength is larger than the fiber-core diameter. The other uncertainties are the misalignment in the

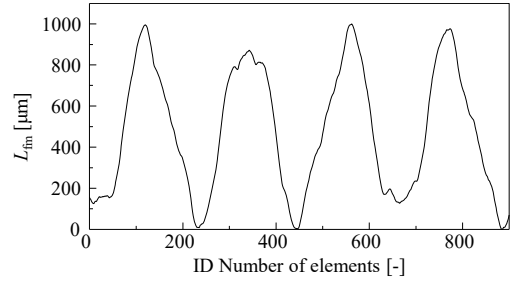
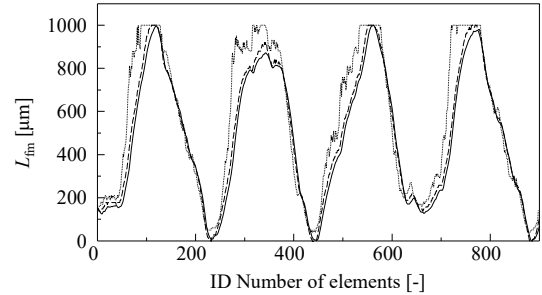


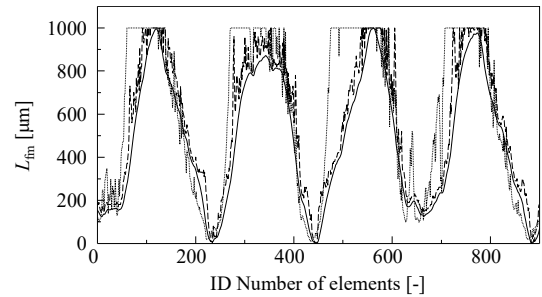
Fig. 19. Simulated random wave.

TABLE II
COMPARISON OF MEASURED VALUE

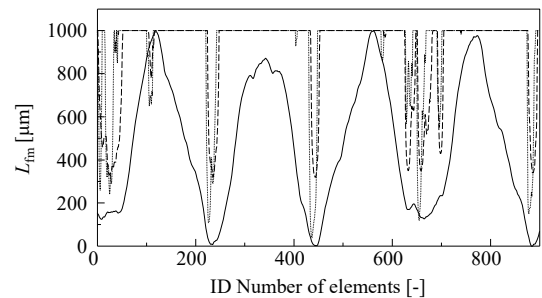
	W_{fm} [μm]	Sensor type	Mean thickness [μm]
Origin	-	-	514
FOTP	$10d_{clad}$	0S	540
		1S	592
	d_{clad}	0S	593
		1S	650
$0.1d_{clad}$	0S	908	
	1S	922	



(a) $W_{fm} = 10d_{clad}$



(b) $W_{fm} = d_{clad}$



(c) $W_{fm} = 0.1d_{clad}$

Fig. 20. Comparison of the virtual-film-thickness measurement via 0S- and 1S-type FOTP. Solid line: the original waveform. Dashed/dotted line: the result of the 0S-/1S-type FOTP.

optics and the stability of the intensity meter. It is necessary to confirm the specifications of these optics when the thickness range is below 200 μm in particular.

From the viewpoint of sensor selection, OS is the best for measuring microfilm flows. IS can detect complex waves on a microfilm flow. OG has insufficient sensitivity to the microfilm, but it remains useful in that it maintains a large I_G in the examined sub-mm range. OG could be much more suitable for general liquid-film detection.

Further research will improve the calibration accuracy by the ray-tracing simulation of whole FOTP optics. It might be possible to determine what optics and FOTP sensor should be used and how much precision should be required for assembling. By meeting this challenge, the RTA method could be extended to general optical methods including visualization [41].

REFERENCES

- [1] W. K. Lewis and W. G. Whitman, "Principles of Gas Absorption," *Ind. Eng. Chem.*, Vol. 16, pp. 1215–1220, 1924.
- [2] R. B. Bird, W. E. Stewart, and E. N. Lightfoot, *Transport Phenomena.*, Hoboken, NJ, USA: John Wiley & Sons, 1960, pp. 557.
- [3] S. Komori, R. Nagaosa, and Y. Murakami, "Turbulence structure and mass transfer across a sheared air-water interface in wind-driven turbulence," *J. Fluid Mech.*, Vol. 249, pp. 161–183, Apr. 1993.
- [4] P. N. Yoshimura, T. Nosoko, and T. Nagata, "Enhancement of mass transfer into a falling laminar liquid film by two-dimensional surface waves—Some experimental observations and modeling," *Chem. Eng. Sci.*, Vol. 51, no. 8, pp. 1231–1240, Apr. 1996, DOI: 10.1016/0009-2509(95)00387-8.
- [5] V. E. Nakoryakov, V. V. Ostapenko, and M. V. Bartashevich, "Heat and mass transfer in the liquid film on a vertical wall in roll-wave regime," *Int. J. Heat Mass Transfer*, Vol. 55, no. 23-24, pp. 6514–6518, Nov. 2012, DOI: 10.1016/j.ijheatmasstransfer.2012.06.054.
- [6] K. J. Chu and A. E. Dukler, "Statistical characteristics of thin, wavy films: part II. Studies of the substrate and its wave structure," *AIChE J.* Vol. 20, pp. 695–706, Jul. 1974, DOI: 10.1002/aic.690200410.
- [7] G. F. Hewitt, A. H. Govan, "Phenomenological modelling of non-equilibrium flows with phase change," *Int. J. Heat Mass Transfer*, Vol. 33, no. 2, pp. 229–242, Feb. 1990, DOI: 10.1016/0017-9310(90)90094-B.
- [8] I. Tanasawa, "Advances in condensation heat transfer," *Adv. Heat Transf.*, Vol. 21, pp. 55–139, 1991, DOI: 10.1016/S0065-2717(08)70334-4.
- [9] T. Fukano, S. Mori, S. Akamatsu, and A. Baba, "Relation between temperature fluctuation of a heating surface and generation of drypatch caused by a cylindrical spacer in a vertical boiling two-phase upward flow in a narrow annular channel," *Nucl. Eng. Des.*, Vol. 217, no. 1-2, pp. 81–90, May 2002, DOI: 10.1016/S0029-5493(02)00159-0.
- [10] H. Anglart, "Progress in understanding and modelling of annular two-phase flows with heat transfer," *Nucl. Eng. Des.*, Vol. 345, no. 15, pp. 166–182, Apr. 2019, DOI: 10.1016/j.nucengdes.2019.02.007.
- [11] F. G. Hammit, S. Krzeczowski, and J. Krzyzanowski, "Liquid film and droplet stability consideration as applied to wet steam flow," *Forsch. Ing.-Wes.*, Vol. 47 no. 1, pp. 1–36, Jan. 1981, DOI: 10.1007/BF02560457.
- [12] F. Maroteaux, D. Llory, J-F. Le Coz, and C. Habchi, "Liquid Film Atomization on Wall Edges—Separation Criterion and Droplets Formation Model," *J. Fluids Eng.*, Vol. 124, no. 3, pp. 565–575, Sep. 2002, DOI: 10.1115/1.1493811.
- [13] M. A. Friedrich, H. Lan, J. L. Wegener, J. A. Drallmeier, and B. F. Armaly, "A Separation Criterion With Experimental Validation for Shear-Driven Films in Separated Flows," *J. Fluids Eng.*, Vol. 130, no. 5, 051301 (9 pages), May 2008, DOI: 10.1115/1.2907405.
- [14] F. F. Lapp, S. Hecker, S. Schuster, and D. Brillert, "The Multi-Phase Flow Test Facility "EMMA" to Investigate Local Heat Transfer Coefficients and Liquid Water Films at Wet Steam Conditions," presented at ASME Turbo Expo 2020, Virtual, Online, Sep. 21–25, 2020.
- [15] N. Handa, H. Hiyama, K. Amagai, and A. Yano, "Experimental and modelling investigation of re-adhesion mechanism of detached nanoparticles to wafer surface in spin rinse process," *ECS J. Solid State Sci. Technol.*, Vol. 9, no. 6, 064001, Jul. 2020.
- [16] S. Beamish, X. Li, H. Brunskill, A. Hunter, and R. Dwyer-Joyce, "Circumferential film thickness measurement in journal bearings via the ultrasonic technique," *Tribol. Int.*, Vol. 140, 106295, Aug. 2020, DOI: 10.1016/j.triboint.2020.106295.
- [17] P. A. Flournoy, R. W. McClure, and G. Wyntjes, "White-Light Interferometric Thickness Gauge," *Appl. Opt.*, Vol. 11, no. 9, pp. 1907–1915, 1972, DOI: 10.1364/AO.11.001907.
- [18] C. Lin and R. F. Sullivan, "An Application of White Light Interferometry in Thin Film Measurements," *IBM J. Res. Dev.*, Vol. 16, no. 3, pp. 269–276, May 1972, DOI: 10.1147/rd.163.0269.
- [19] H. Fujiwara, *Spectroscopic Ellipsometry: Principles and Applications.* Hoboken, NJ, USA: John Wiley & Sons, 2007, pp. 81–140.
- [20] K. Javdani, "Mass transfer in wavy liquid films," *Chem. Eng. Sci.*, Vol. 29, no. 1, pp. 61–69, Jan. 1974, DOI: 10.1016/0009-2509(74)85030-X.
- [21] T. Kamei and A. Serizawa, "Measurement of 2-dimensional local instantaneous liquid film thickness around simulated nuclear fuel rod by ultrasonic transmission technique," *Nucl. Eng. Des.*, Vol. 184, no. 2–3, pp. 349–362, Aug. 1998, DOI: 10.1016/S0029-5493(98)00208-8.
- [22] T. Hazuku, T. Takamasa, and Y. Matsumoto, "Experimental study on axial development of liquid film in vertical upward annular two-phase flow," *Int. J. Multiph.*, Vol. 34, pp. 111–127, Oct. 2007, DOI: 10.1016/j.ijmultiphaseflow.2007.10.008.
- [23] B. Hu, C. Stewart, C. P. Hale, C. J. Lawrence, A. R. W. Hall, H. Zwiens, and G. F. Hewitt, "Development of an X-ray computed tomography (CT) system with sparse sources: application to three-phase pipe flow visualization," *Exp. Fluids*, Vol. 39, pp. 667–678, Jun. 2005, DOI: 10.1007/s00348-005-1008-2.
- [24] O. Skjæråasen and N. R. Kesana, "X-ray measurements of thin liquid films in gas-liquid pipe flow," *Int. J. Multiph.*, Vol. 131, 103391, Oct. 2020, DOI: 10.1016/j.ijmultiphaseflow.2020.103391.
- [25] T. Fukano, "Measurement of time varying thickness of liquid film flowing with high speed gas flow by a constant electric current method (CECM)," *Nucl. Eng. Des.*, Vol. 184, no. 2–3, pp. 363–377, Oct. 1998, DOI: 10.1016/S0029-5493(98)00209-X.
- [26] K. Ohba, T. Origuchi, and Y. Shimanaka, "Multi-Fiber Optic Liquid Film Sensor. I," in *Proc. 4th Sensor Symp.*, 1984, pp. 33–37.
- [27] R. J. Goldstein, "Fluid mechanics measurements," in *Shadowgraph System*, 2nd ed., Philadelphia, PA, USA: Taylor & Francis, 1996, pp. 471–473.
- [28] N. Otsu, "A threshold selection method from gray-level histograms," *IEEE Trans. Sys. Man. Cyber.* Vol. 9, no. 1, pp. 62–66, 1979, DOI:10.1109/TSMC.1979.4310076.
- [29] S. V. Alekseenko, A. V. Bobylev, A. R. Evseev, V. M. Karsten, D. M. Markovich, and B. V. Tarasov, "Measurements of the Liquid-Film Thickness by a Fiber-Optic Probe," *Instrum. Exp. Tech.*, Vol. 46, no. 2, pp. 260–264, Mar. 2003, DOI: 10.1023/A:1023650623759.
- [30] D. V. Zaitsev, O. A. Kabov, and A. R. Evseev, "Measurement of locally heated liquid film thickness by a double-fiber optical probe," *Exp. Fluids*, Vol. 34, pp. 748–754, May 2003, DOI: 10.1007/s00348-003-0621-1.
- [31] G. Perrone and A. Vallan, "A Low-Cost Optical Sensor for Noncontact Vibration Measurements," *IEEE Trans. Instrum. Meas.*, Vol. 58, no. 5, pp. 1650–1656, May 2009, DOI: 10.1109/TIM.2008.2009144.
- [32] Md. M. Hossain, G. Lu, and Y. Yan, "Optical Fiber Imaging Based Tomographic Reconstruction of Burner Flames," *IEEE Trans. Instrum. Meas.*, Vol. 61, no. 5, pp. 1417–1425, May 2012, DOI: 10.1109/TIM.2012.2186477.
- [33] T. Saito, K. Matsuda, Y. Ozawa, S. Oishi, and S. Aoshima, "Measurement of tiny droplets using a newly developed optical fibre probe micro-fabricated by a femtosecond pulse laser," *Meas. Sci. Technol.*, Vol. 20, no. 11, 114002, Nov. 2009, DOI: 10.1088/0957-0233/20/11/114002.
- [34] Y. Mizushima and T. Saito, "Detection method of a position pierced by a single-tip optical fibre probe in bubble measurement," *Meas. Sci. Technol.*, Vol. 23, no. 8, 085308, Aug. 2012, DOI: 10.1088/0957-0233/23/8/085308.
- [35] A. Sakamoto and T. Saito, "Computational analysis of responses of a wedge-shaped-tip optical fiber probe in bubble measurement," *Rev. Sci. Instrum.*, Vol. 83, 075107, 2012, DOI: 10.1063/1.4732819.

- [36] Y. Mizushima, A. Sakamoto, and T. Saito, "Measurement technique of bubble velocity and diameter in a bubble column via Single-Tip Optical-fiber Probing with judgment of the pierced position and angle," *Chem. Eng. Sci.*, Vol. 100, no. 30, pp. 98–104, 2013, DOI: 10.1016/j.ces.2013.01.046.
- [37] Y. Mizushima and T. Saito, "Improving the Accuracy of Droplet Measurement by Optical Fiber Probe Using 3D Ray-Tracing Simulation," *J. Chem. Eng. Japan*, Vol. 52, no. 2, pp. 171–178, Feb. 2019, DOI: doi.org/10.1252/jcej.17we211.
- [38] K. Yamaguchi, T. Sanada, and Y. Mizushima, "Accurate thin-film measurement method based on a distribution of laser intensity emitted from optical fiber: Proposal of step light emitted model for ray-tracing simulation," *Mech. Eng. Lett.*, Vol. 6, 20-00419, Nov. 2020, DOI: 10.1299/mel.20-00419.
- [39] A. Sommerfeld, and J. Runge, "Anwendung der Vektorrechnung auf die Grundlagen der geometrischen Optik," *Ann. Phys.*, Vol. 340, pp. 277–298, 1911, DOI: doi.org/10.1002/andp.19113400705.
- [40] E. Bianciardi and V. Rizzoli, "Propagation in graded-core fibres: a unified numerical description," *Opt. Quantum Electron.*, Vol. 9, pp. 121–133, Mar. 1977, DOI: 10.1007/BF00619892.
- [41] E. Luthman, N. Cymbalist, D. Lang, G. Candler, and P. Dimotakis, "Simulating schlieren and shadowgraph images from LES data," *Exp. Fluids*, Vol. 60, 134, Jul. 2019, DOI: 10.1007/s00348-019-2774-6.



Yuki Mizushima was born in Shizuoka, Japan, in 1988. He received the B.S., M.S., and the Dr. Tech. degree in mechanical engineering from Shizuoka University, Shizuoka, Japan, in 2011, 2013, and 2016, where he focused on fiber-optic measurement in multiphase flows.

From 2016 to 2019, he was with Ebara Corporation, Kanagawa, Japan, where he was involved in the development of the optical measurement of vibration from rotating machinery. Since 2019, he has been an Assistant Professor with the Mechanical Engineering Department, Shizuoka University. His current research interests include ray-tracing simulation, laser-based flow measurement, optical waveguides, and gas-liquid two-phase flows.